

Assessing Moonlight Availability for Nighttime Environmental Applications by Low-Light Visible Polar-Orbiting Satellite Sensors

STEVEN D. MILLER, CYNTHIA L. COMBS, AND STANLEY Q. KIDDER

Cooperative Institute for Research in the Atmosphere, Fort Collins, Colorado

THOMAS F. LEE

Naval Research Laboratory, Monterey, California

(Manuscript received 12 October 2011, in final form 13 December 2011)

ABSTRACT

The next-generation U.S. polar-orbiting environmental satellite program, the Joint Polar Satellite System (JPSS), promises unprecedented capabilities for nighttime remote sensing by way of the day/night band (DNB) low-light visible sensor. The DNB will use moonlight illumination to characterize properties of the atmosphere and surface that conventionally have been limited to daytime observations. Since the moon is a highly variable source of visible light, an important question is where and when various levels of lunar illumination will be available. Here, nighttime moonlight availability was examined based on simulations done in the context of Visible/Infrared Imager Radiometer Suite (VIIRS)/DNB coverage and sensitivity. Results indicate that roughly 45% of all JPSS-orbit [sun-synchronous, 1330 local equatorial crossing time on the ascending node (LTAN)] nighttime observations in the tropics and midlatitudes would provide levels of moonlight at crescent moon or greater. Two other orbits, 1730 and 2130 LTAN, were also considered. The inclusion of a 2130 LTAN satellite would provide similar availability to 1330 LTAN in terms of total moonlit nights, but with approximately a third of those nights being additional because of this orbit's capture of a different portion of the lunar cycle. Nighttime availability is highly variable for near-terminator orbits. A 1-h shift from the 1730 LTAN near-terminator orbit to 1630 LTAN would nearly double the nighttime availability globally from this orbit, including expanded availability at midlatitudes. In contrast, a later shift to 1830 LTAN has a negligible effect. The results are intended to provide high-level guidance for mission planners, algorithm developers, and various users of low-light applications from these future satellite programs.

1. Introduction: Historical perspective on satellite-based low-light visible radiometer technology

Daytime measurements of reflected sunlight in the visible spectral band (i.e., wavelengths between 0.4 and 0.7 μm) offer a wide assortment of information about the physical environment. The high degree of scattering by liquid and ice clouds in the visible band provides sensitivity to a large range of cloud water content, in contrast to the thermal infrared where liquid and ice absorption are strong and sensitivity falls off rapidly with increasing cloud optical thickness. Low clouds and

fog, often obscured in infrared-window (e.g., 11 μm) imagery for lack of temperature contrast against the surface, are readily detected in visible-band imagery owing to their strong reflectance contrast against most relatively dark terrestrial backgrounds. Atmospheric aerosols (e.g., mineral dust, pollution, smoke from biomass burning, and volcanic ash plumes) are often too tenuous to be detected at infrared wavelengths, but are readily observable in the visible. At the surface, visible-band reflectance allows for discrimination of snow cover, and highly sensitive subbands enable the characterization of phytoplankton blooms and water turbidity in littoral zones. In comparison to thermal infrared measurements from a typical cross-track scanning satellite radiometer, the strength of visible-band sunlight provides higher signal-to-noise ratios at shorter integration times, enabling measurements at higher spatial resolution and commensurately better interpretation of environmental features.

Corresponding author address: Steven D. Miller, Cooperative Institute for Research in the Atmosphere, Colorado State University, Foothills Campus, 1375 Campus Delivery, Fort Collins, CO 80523-1375.
E-mail: miller@cira.colostate.edu

In the early 1960s during the “space race” era, the Television and Infrared Observation Satellite (TIROS) Civilian Program began collecting the first daytime visible imagery of the Earth and its weather, including daytime visible measurements. A wide assortment of contemporary environmental satellites [both low-Earth-orbiting (LEO) and geostationary (GEO)] continues the legacy of TIROS, carrying optical-spectrum radiometers with one or more daytime visible bands. The visible band (conventionally referring to narrowband channels centered near $0.65 \mu\text{m}$ in the “red” part of the optical spectrum) has been a mainstay of satellite-based imagery ever since. Here, measurements for a typical sunlight illuminated scene are of the order $1\text{--}100 \text{ W m}^{-2} \text{ sr}^{-1} \mu\text{m}^{-1}$. While limited energy at visible wavelengths exists at night, the signals are far below the sensitivity of conventional visible-band sensors, relegating these sensors useless during the nighttime hours.

Not long after the TIROS program began, a Department of Defense (DoD) program under the auspices of the U.S. Air Force joined the emerging constellation of polar-orbiting weather satellites. Initially a classified program, the principal focus of this Defense Meteorological Satellite Program (DMSP; Dickinson et al. 1974) was on day/night cloud analyses and “first light” (i.e., early dawn) imaging capabilities for cloud forecasting. For this reason, members of the DMSP constellation have traditionally been placed in near-terminator to late-morning orbits. DMSP was declassified in 1972 and continues as an operational program, with data being available to the broader civilian/scientific community through the National Oceanic and Atmospheric Administration (NOAA; Allison 1980). Since 1976, each member of the DMSP constellation beginning with satellite *DMSP-F1* on Block 5D-1 has been equipped with an Operational Linescan System (OLS) imaging radiometer that provides two broad spectral bands in the visible/near-infrared (VNIR; $\sim 0.5\text{--}0.9 \mu\text{m}$) and the thermal infrared (TIR; $\sim 10\text{--}13 \mu\text{m}$) over a $\sim 3000\text{-km}$ -wide swath (Lieske 1981). The OLS is tailored to provide sensitivity to the extreme dynamic range in visible light magnitude necessary to meet DoD requirements for cross-terminator imaging, modifying its detection approach across several operating modes (Elvidge et al. 1997). Numerous prime examples of OLS imaging capabilities can be found in Fett et al. (1983) and Johnson et al. (1994).

Unlike conventional visible-band sensors that are capable of providing useful measurements down to levels of perhaps $1\text{--}10 \text{ W m}^{-2} \text{ sr}^{-1} \mu\text{m}^{-1}$, the OLS VNIR band includes a photomultiplier tube (PMT) that is capable of amplifying extremely low visible light signals at night and providing sensitivity down to roughly $10^{-5} \text{ W m}^{-2} \text{ sr}^{-1} \mu\text{m}^{-1}$ —from four to five orders of

magnitude lower than the visible bands designed to measure daytime reflected sunlight. There are significant limitations of the OLS visible band in terms of its radiometric resolution (6-bit quantization), limited calibration (onboard dynamic gain settings are not packaged with the data, based on predicted scene illumination and bidirectional reflectance geometries for the solar and lunar sources), and coarse spatial resolution ($\sim 2.8\text{-km}$ “smooth” data in standard nighttime operating mode). Despite these limitations, the research community has succeeded in exploiting its unique information for numerous qualitative and quantitative nighttime applications. Studies on population density (Sutton et al. 2001), economic activity (e.g., Ebener et al. 2005), and atmospheric emissions (e.g., Toenges-Schuller et al. 2006) use correlations between these parameters and the distribution/intensity of anthropogenic light emissions. Environmental studies related to aerosol properties (Zhang et al. 2008), cloud and snow/ice cover (Foster and Hall 1991; Miller et al. 2005b), and bioluminescence (Miller et al. 2005a) testify to the breadth of possibilities for low-light visible nighttime applications in this field.

Besides the OLS there exist few spaceborne sensors capable of low-light sensing for general environmental applications. The Tropical Rainfall Measuring Mission (TRMM) Lightning Imaging Sensor (LIS; Christian et al. 1999) and the Optical Transient Detector (OTD; Christian et al. 1996) are examples of low-light sensing instruments that are specialized to the task of detecting rapid changes from lightning flashes and other transient luminous events. A professional-grade color camera was operated with image motion compensation on the International Space Station (ISS) to build signal via time integration and demonstrate the capabilities of high spatial resolution information and differentiation between various anthropogenic light emissions—a proof of concept for a possible future space mission with a scientific focus on artificial sources (Elvidge et al. 2007). These ISS camera observations do not constitute calibrated digital data suitable for quantitative applications, however.

Perhaps the closest analog to the DMSP/OLS is the *Satélite de Aplicaciones Científicas-C* [*Satellite Application Satellite-C* (SAC-C), e.g., <http://www.conae.gov.ar/eng/satellites/sac-c.html>], which carries the High Sensitivity Technological Camera (HSTC). The HSTC is designed for nighttime low-light sensing over a 700-km swath at 300-m spatial resolution and a $450\text{--}850$ spectral bandpass. However, to date these data have not been widely available to the research and operational communities. An improved version High Sensitivity Camera (HSC) is now deployed as part of the Aquarius instrument payload on *SAC-D* (launched on

10 June 2011). Also on the horizon is the Korean *Multi-Purpose Geostationary Satellite (MP-GEOSAT)* in the ~2017/18 timeframe, which promises to offer the first geostationary-based low-light imager, the Geostationary Ocean Color Imager-2 (GOCI-2).

In 1993/94, the U.S. government directed NOAA, DoD, and the National Aeronautics and Space Administration (NASA) to converge the operational meteorological satellite programs, leading to the development of a triagency National Polar-orbiting Operational Environmental Satellite System (NPOESS) in 1995. Designated as successor to the Polar-orbiting Operational Environmental Satellite (POES) program and DMSP, the NPOESS constellation was designed to address simultaneously the operational needs of both agencies via an assortment of state-of-the-art remote sensing instruments. The originally proposed program consisted of a three-satellite constellation with local time ascending nodes (LTANs) of 1330, 1730, and 2130, providing roughly 4-hourly revisits to a given location at mid-latitudes. The low-light visible imaging requirement came across from the DoD side to provide continuity to the DMSP/OLS capability. The optical-spectrum radiometer envisioned for NPOESS was the Visible/Infrared Imager Radiometer Suite (VIIRS), which would include a day/night band (DNB) sensor specially tailored to low-light visible imaging requirements.

After a restructuring of NPOESS to address growing budgetary issues, the program demanifested the midmorning/evening (0930 descending/2130 ascending) orbit in favor of leveraging the European Organisation for the Exploitation of Meteorological Satellites (EUMETSAT) program and its Meteorological Operation (MetOp) satellite as part of the Initial Joint Polar System (IJPS) coordination between NOAA and EUMETSAT. MetOp flies in the same midmorning/evening orbit planned originally for NPOESS, carrying an Advanced Very High Resolution Radiometer (AVHRR) instrument as its optical-spectrum payload, identical to those carried on the current generation of NOAA/POES satellites. While MetOp does not include a low-light visible band, there are considerations for including such a capability on the follow-on EUMETSAT Polar System (PostEPS). While NPOESS was subsequently cancelled in 2010, elements of its original vision and design will be realized on the satellites of the Joint Polar Satellite System (JPSS) program, with a precursor "NPOESS" Preparatory Project (NPP) risk-reduction satellite (led by NASA) launched on 28 October 2011. The introduction to the broader meteorological satellite operational user community of low-light visible measurements, and the design of a fully calibrated version of it paired with multispectral observations in the

thermal/near-infrared, may yet prove a lasting positive legacy of NPOESS.

This paper focuses on the potential application of future low-light visible capabilities from operational environmental satellites, and in particular, addresses the question of where and when nighttime applications requiring the presence of moonlight can be attempted. By complement, the findings pertain also to where/when nighttime applications requiring the *absence* of moonlight (e.g., terrestrial emissions) may be attempted from these same satellites. The following specific questions are addressed by this research: 1) Considering the VIIRS/DNB placed in selected orbits, what is the total fraction of global nighttime data that offers detectable levels of reflected moonlight? 2) How does this fraction vary spatially, seasonally, and with a threshold for lunar irradiance? 3) What is gained by including a low-light sensor on the 2130 LTAN orbit? 4) What is the sensitivity of nighttime lunar availability for the VIIRS/DNB in near-terminator orbits? We attempt to answer these questions quantitatively, via a statistical analysis done on combined orbital and lunar models.

The paper is structured as follows: section 2 gives an overview of the VIIRS/DNB. Section 3 reviews essential considerations for characterizing the variability of moonlight over space and time. Section 4 examines the geometry of the NPP/JPSS and various other sun-synchronous orbits. Section 5 addresses the problem of "lunar availability." Section 6 presents selected results of lunar simulations to understand the general latitudinal and seasonal dependencies of moonlight as well as the advantages of sampling across the lunar cycle. Section 7 extends this analysis to 5-yr detailed orbital/sensor simulations of lunar availability for various orbits. Section 8 gives special attention to the near-terminator orbit and considers the merits of a proposed 1-h temporal shift of the orbital plane. Section 9 summarizes and concludes the paper.

2. VIIRS and the day/night band

VIIRS has 22 bands spanning 0.4–12.0 μm , including the single broadband (400–1100-nm spectral range, with ~500–900 nm at full-width half-maximum response) low-light DNB sensor. The DNB uses time-delay integration (TDI) on a charge-coupled device (CCD) and a 64-stage multidetector aggregation strategy to provide similar sensitivity to the OLS low-light band at a nearly constant pixel resolution of 740 m across the entire 3000-km swath. The data are collected simultaneously at three stages (low/mid/high) of gain, with the unsaturated stage selected dynamically for each pixel to achieve a dynamic range spanning over seven orders of magnitude (down to a minimum detectable in-band radiance of $\sim 10^{-5} \text{ W m}^{-2} \text{ sr}^{-1}$).

While the sensitivity is similar to that of the DMSP/OLS, the improved radiometric resolution (14-bit digital number quantization versus only 6-bit for the OLS) combined with its dramatically improved spatial resolution make for a remarkably improved capability. Lee et al. (2006) provide an overview of the VIIRS/DNB and some of its anticipated improved capabilities based in part on demonstrations of current meteorological applications with the DMSP/OLS as well as considerations of the new technology being implemented.

Current and future VIIRS sensors fly on satellites in conventional sun-synchronous orbits with a nominal altitude above mean sea level of ~ 824 km (providing a 101-min orbital period, or ~ 14.4 orbits per day, with a 16-day ground-track repeat cycle) and provide a ~ 3000 -km-wide swath of imagery along the ground track. In a sun-synchronous orbit the satellite's orbital plane precesses about the Earth's spin axis at a rate that matches the average rate at which Earth moves in its orbit about the sun (360° per year). As a result, the angle in the Earth's equatorial plane formed between the mean sun location (equator; local noon) and the location where the satellite ascends northward (or descends southward) across the equator (called ascending or descending "nodes" of the orbit) remains nearly constant. It also means that the local time of these nodes [referred to as the equatorial crossing times (ECTs)] is constant.

The LTAN referred to throughout the course of this paper is defined mathematically as

$$\text{LTAN} = 12 + (\lambda_{\text{AN}} - \lambda_{\text{Sun}})/15, \quad (1)$$

where λ_{AN} is the longitude of the ascending node location and λ_{Sun} is the longitude of the mean sun location. LTAN is measured in hours [and noted in hours and minutes (HHMM)] and the longitudes are measured in degrees (Kidder and Vonder Haar 1995). The constant value of 15 arises from the fact that the Earth rotates 15° per hour (i.e., full rotation of 360° in a 24-h period, ignoring the details of the sidereal day) with respect to the mean sun. The constant value of 12 refers to the mean sun at local noon. Since the ECT is constant for sun-synchronous orbits, it is often used in reference to the orbits. By convention, a sun-synchronous satellite orbit is referred to by its ascending-node ECT. Hereafter, the "LTAN" will be taken as implied when referring to the orbits (i.e., 1330 LTAN will be referenced hereafter as the 1330 orbit, etc.).

3. The moon as a nocturnal source of visible light

Unlike the sun, the moon is a highly variable source of visible light since it is a variable reflector of sunlight.

Factors affecting lunar brightness (listed in order from greatest to least importance) include the lunar phase, the moon–Earth distance, the moon–sun distance, and libration (slight changes in the Earth-facing portion of the lunar disk over time, which in turn lead to slight variations in the lunar albedo, owing to the spatially heterogeneous lunar surface reflectance). Of course, at a given location/time the altitude angle of the moon will determine the amount of horizontal lunar irradiance available for illumination. Miller and Turner (2009) provide a review of these factors and their impacts on predicting the lunar irradiance.

The lunar orbit is complex. The illuminated portion of the moon as viewed from Earth varies across the lunar cycle (approximately 29 days and 13 h when accounting for the orbit of the Earth/moon system around the sun), defining the "phases" waxing/waning between new and full moon (see Fig. 1). The lunar orbit is highly elliptical compared to the Earth's orbit about the sun, resulting in full moons at lunar perigee being much brighter than full moons occurring at lunar apogee. It exhibits a highly varying declination range (between 37° and 57°) over the course of the lunar cycle, and the sublunar position can extend beyond the Tropics of Cancer and Capricorn since the orbital plane is tilted $\sim 5.9^\circ$ with respect to the ecliptic. Since the full moon is by geometric definition always opposite the sun, at midlatitudes the summertime full moon is typically much lower on the horizon than during wintertime. Also, the full moon is much brighter than the quarter moon (roughly 9 times brighter) even though the surface area is only about twice as large; it is postulated that as the phase angle approaches 0° , the shadows produced by lunar craters and ridges are minimized—a phenomenon called the opposition surge (Buratti et al. 1996).

This is all to say that predicting the moon's sky position and brightness, both in a general sense and specifically at a particular surface location on any given night, is a highly nonlinear and hence nontrivial task that requires the assistance of an astronomical model. For this work, we predict the sun/moon position and twilight illumination conditions (necessary for determining astronomical dark, which is our criterion for "night") using the Solar-Lunar Almanac Core (SLAC) model (J. A. Bangert 1998, unpublished manuscript) developed by the U.S. Naval Observatory's Astronomical Applications Department. The SLAC model is used to compute the local solar/lunar geometry at each sample location in the orbital/swath simulation model described in section 7 below.

In addition to geometry information, the SLAC model provides a general sense for moonlight intensity via a crude estimate of the illuminance (a photometric

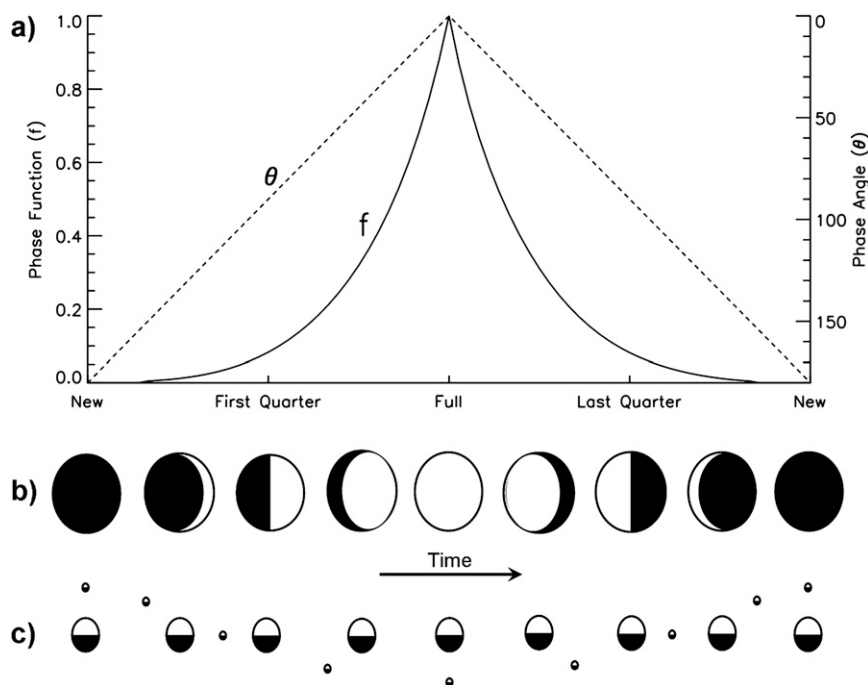


FIG. 1. (a) Evolution of the lunar phase angle (θ) and phase function (f) over the course of the lunar cycle, (b) changing appearance of the lunar disk as seen from Earth, and (c) Earth-moon geometry (not drawn to scale) as viewed above the North Pole of Earth (with sunlight originating from top of page). In (b) and (c), illuminated sides of bodies are shown in white and shaded sides in black. (From Miller and Turner 2009.)

quantity in units of luxes that is correlated with the brightness perception of the human eye) based on fits to model data of Brown (1952; J. A. Bangert 2011, personal communication). The value is not spectral and is insufficient for relating to VIIRS/DNB sensitivity thresholds in a quantitative way. A more robust and detailed specification of the top-of-atmosphere, downwelling lunar spectral irradiance (in units of $\text{mW m}^{-2} \mu\text{m}^{-1}$) for a given date/time is required to assess whether or not the amount of moonlight will be sufficient for quantitative nighttime applications. Kieffer and Stone (2005) provide an empirically based spectral irradiance model, based on photometric observations from the ground-based Robotic Lunar Observatory (ROLO) program at the U.S. Geological Survey in Flagstaff, Arizona. The model is spatially resolved (capturing the details of lunar *maria* and *terrae*) and has been used extensively, by design, for spaceborne imaging instrument calibration of visible-band sensors during “moon-look” exercises.

For the current work, we regarded the moon as a single (spatially integrated) source of illumination whose spectral irradiance is principally a function of lunar phase and the moon/Earth/sun geometry (libration effects are neglected). We enlisted the simple lunar spectral irradiance prediction model described by Miller and Turner (2009), preconvolved to the spectral response

function of the VIIRS/DNB (cf. Fig. 4 of Miller and Turner 2009). This irradiance model, which has been validated against both ROLO and satellite-based lunar views, accepts time-dependent information on the lunar phase angle, sun–Earth distance, and moon–Earth distance as provided by the SLAC lunar model. The uncertainty in the irradiance model ranges from about 7% to 12% for typical observing conditions, and may serve as a useful benchmark for assessing what levels of moonlight are sufficient for a specific quantitative application. Thus, all the necessary information for assessing day/night conditions and moonlight irradiance was available for any location and time. In the current assessment of VIIRS/DNB lunar availability, the space/time sampling was determined by the orbital geometry and sensor swath characteristics.

4. Nighttime observations as a function of satellite orbital geometry

It is important to understand the geometric relationship between the location of the sun and the VIIRS/DNB swath for the purpose of knowing when and where the low-light sensor will observe points that are on the night hemisphere of the Earth, and how far from the day/night terminator those points lie (i.e., how dark they

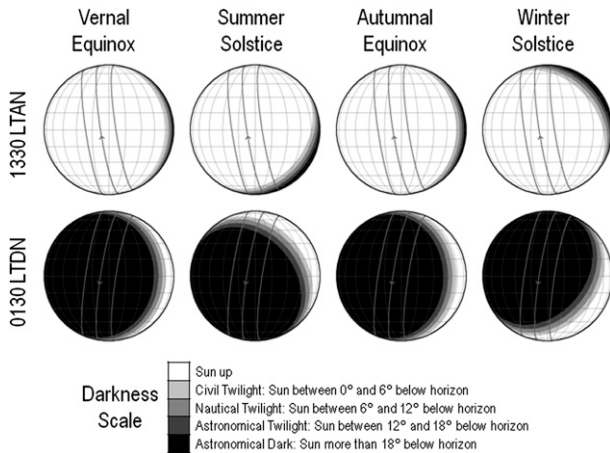


FIG. 2. Orbital track, 3000-km swath (VIIRS), and degrees of darkness for a sun-synchronous satellite with a 1330 LTAN. Arrow along subsatellite ground track denotes direction of travel.

are). Under the assumption of sun-synchronous polar orbits, the relationship is a strong function of the crossing time (e.g., LTAN) and latitude (through seasonal changes to the orientation of the terminator) but will be independent of longitude. This allows us to present results as a function of latitudinal zone and season.

Figures 2–4 compare the darkness pattern with the satellite ground track (defining the intersection of the Earth’s surface and the line between the satellite position and the center of the Earth) assuming the 3000-km VIIRS/DNB swath width for sun-synchronous satellites with LTANs of 1330, 1730, and 2130 (the originally scoped NPOESS constellation), respectively. Drawn in these figures are the ascending and descending ground tracks of each satellite. Various gray shades denote different categories of darkness ranging from daytime (sun above horizon) to astronomical darkness (sun below the horizon by 18° or more, at which point atmospheric molecular scatter no longer produces twilight conditions). For the purposes of this analysis and all subsequent results, we considered night as pertaining to the definition of astronomical darkness, realizing that the day/night terminator is not a discrete step function but rather a gradual transition through twilight (owing to the scattering atmosphere). The grounds for this definition stem from our specific interest in the unambiguous use of moonlight for nighttime environmental applications. In particular, beyond the problems introduced by dual (sun/lunar) illumination, we wish to avoid illumination conditions that are difficult to account for in physical retrieval algorithms because of their associated long photon pathlengths through the atmosphere and significant 3D effects (shadows, side illumination of clouds, terrain, etc.).

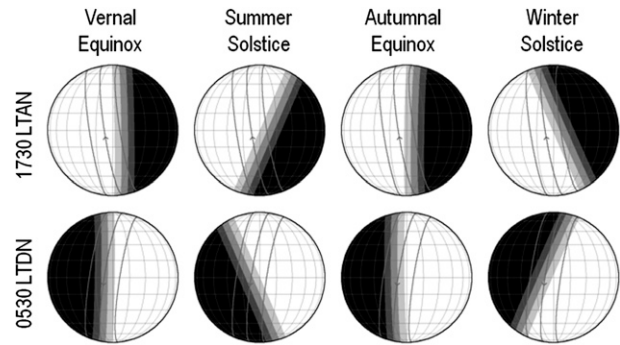


FIG. 3. As in Fig. 2, but for a sun-synchronous satellite with a 1730 LTAN.

Since sun-synchronous satellites move with the *annual mean sun* (i.e., as if the Earth were in a circular orbit around the sun, progressing at the same angular distance each day), the spatial distribution of darkness changes slowly through the year. In the north/south direction, the darkness pattern changes according to the sun’s changing declination angle ($\pm 23.5^\circ$). In the east/west direction the darkness pattern changes as the current day’s sun longitudinal position deviates slightly from that of the annual mean sun because of the Earth’s 23.4° axial tilt and its elliptical (eccentricity of 0.017) orbit around the sun (we will show later why this is an important consideration for near-terminator orbital configurations). The analemma (e.g., Oliver 1972) describes these small deviations in latitude/longitude of the subsolar point from its mean position at a given time of day. During a particular day, to good approximation, each orbit of the satellite maintains essentially the same geometrical relationship with that day’s darkness pattern.

Figures 2 and 4 show that satellites in the 1330 and 2130 orbital configurations offer numerous observations in the dark portions of the Earth for each orbit. The locations of the darkness patterns change with season in familiar ways. For example, near the solstices, the summer pole is never observed in darkness and the winter

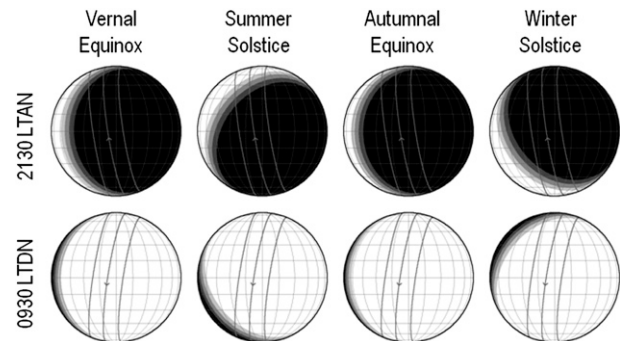


FIG. 4. As in Fig. 2, but for a satellite with a 2130 LTAN.

pole resides in perpetual darkness. The 1730 orbit (Fig. 3), being near the terminator, offers fewer observations of astronomical darkness. In particular, there are almost no observations of the dark tropics, and because of its orbital configuration there are fewer dark observations of the Northern Hemisphere. Whereas very high latitudes of both poles are observed in darkness reasonably often during winter, there is preferential frequency in the Southern Hemisphere winter owing to the 98° inclination of the sun-synchronous orbit, as observed in Fig. 3.

5. Defining a metric for lunar availability

Whereas a very rough estimate of the minimum detectable signal for the VIIRS/DNB is $0.01 \text{ mW m}^{-2} \mu\text{m}^{-1}$, this should not be considered as the threshold signal that enables lunar applications. Various environmental applications will require different levels of the moonlight signal-to-noise ratio (SNR). Instead of attempting to specify a single value for a useful level of moonlight, we report instead the results of these simulations as a function of varying levels of downwelling, top-of-atmosphere moonlight that can be related to the overhead moon at different phases in the lunar cycle. It should be understood that these levels of moonlight can be attained by various combinations of lunar phase, lunar elevation, and moon–Earth distance. For example, a quarter-phase moon directly overhead may produce the same downwelling irradiance as the full moon near the horizon (i.e., at lower lunar elevation, resulting in a cosine-weighted suppression of the full moon irradiance at the current location; Miller and Turner 2009). The actual amount of reflected moonlight measured at the sensor will vary according to the target bidirectional reflectance distribution function (BRDF; noting that snow/ice/cloud albedo ranges over ~30%–90%, and land surfaces ~10%–40%).

The following lunar irradiances (all in units of $\text{mW m}^{-2} \mu\text{m}^{-1}$), weighted by the cosine of the lunar zenith angle and convolved to the DNB sensor response function, were selected as thresholds: 0.05, 0.40, and 1.30. The selected threshold values correspond, roughly and respectively, to the crescent, quarter, and gibbous phases of the lunar cycle. Again, these are notional relationships; the actual magnitude of moonlight measured will be a strong function of the target (cloud, surface, etc.) albedo. The typical range for in-band lunar irradiance for the DNB, ranging from new moon to full moon, is $[0, 3.7 \text{ mW m}^{-2} \mu\text{m}^{-1}]$. Quarter moon illumination has long been regarded as the standard minimum threshold for nighttime lunar applications from the OLS (e.g., Foster and Hall 1991), and will be adopted here as the baseline for the most useful lunar applications.

However, improved signal-to-noise ratio, radiometric resolution, and other sensor improvements compared to the OLS (Lee et al. 2006) may allow for some nighttime applications to be pursued at much lower thresholds of lunar illumination, perhaps those corresponding to the crescent moon.

6. General considerations of orbit when sampling the lunar cycle

The original scope of the NPOESS program called for a midmorning/midevening orbit as part of the three-orbit constellation. In the JPSS program, the first pure-night DNB observations for a given evening will not be available until 0130 local time. Since MetOp does not include a low-light imager, there will be a significant temporal gap from the last available daytime visible imagery. A less obvious impact of losing the 2130 orbit is that fewer nights over the course of the year will have sufficient moonlight for applications. To illustrate this latter point, the SLAC model was run for an arbitrary lunar cycle, and the lunar-phase/geometry results were subsequently passed to the lunar irradiance model of Miller and Turner (2009) to contrast observations collected at 2130 and 0130 (early morning hours of the same night).

Figure 5 shows the results of this simple exercise for a full lunar cycle occurring in December 2011. The 2130 observations represent the contribution of moon phases during the waxing part of the cycle—that set in the west before 0130 (later that same night). In contrast, the 0130 observations capture the waning-side moons that rise in the east after the 2130 (from earlier in the evening) pass. Translating this back to the satellite constellation, this means that the 1330 (which provides the 0130 local crossing at night) and 2130 orbits in tandem would observe a greater number of “lunar nights” across the lunar cycle than either would on its own. There would also be periods when both orbits capture the same lunar nights but at different magnitudes of lunar irradiance because of differences in the lunar zenith angle at the time of the satellite overpass.

We computed the additional number of lunar nights meeting our irradiance threshold by combining the 2130 observations with the 0130 observations, through a 5-yr SLAC simulation for the years 2011–15. We selected a set of sample locations along the prime meridian (local time = UTC) with equal 15° latitudinal spacing between 75°S and 75°N. For each day, information related to the solar/lunar geometry and lunar phase was computed for 1330, 0130, 0930, and 2130 local time (to account for possible nighttime observations on either the ascending or descending nodes for hypothetical satellite

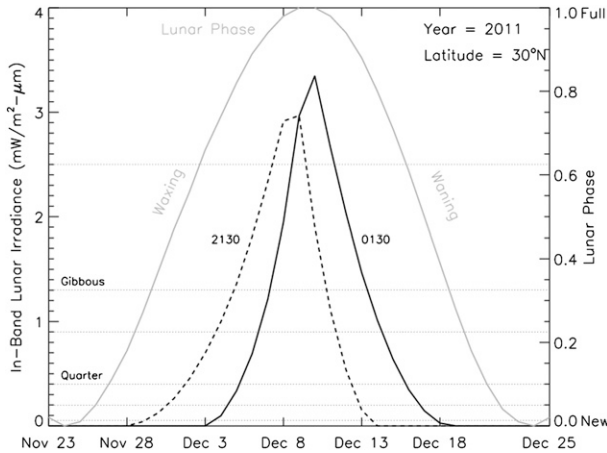


FIG. 5. Depiction of a single lunar cycle for December 2011, and the magnitudes of lunar irradiance as would be measured by a VIIRS/DNB sensor for two different times of the night during this month.

orbits), and these data were input to the lunar irradiance model of Miller and Turner (2009) to provide VIIRS/DNB-equivalent values weighted by the cosine of the lunar zenith angle. The fraction of nighttime lunar irradiance observations that exceeded a given threshold was computed and then multiplied by the total number of nights per year at each latitude to yield the total number of lunar nights per year. To assess the overall availability of data, the number of lunar nights per year is more meaningful than the fraction of lunar nights because the former accounts for latitudinal variation in the number of dark nights. For example, considering the 0130 local times, there are 365 dark nights per year in the tropics but only 304 dark nights per year at 60°N.

Figure 6 indicates the number of nights per year that are potentially available for moonlight applications. Figure 6a shows the number of lunar nights encountered at 0130/1330 local times for various thresholds of lunar irradiance, and Fig. 6b shows the total number of lunar nights when including additional night observations from the 0930/2130 local times. On these additional nights, the 0930/2130 observations exceeded the lunar threshold while those collected at 0130/1330 did not. For the 0130/1330 local times, there were 164 nights per year at the equator with moonlight of at least crescent-moon-equivalent ($0.05 \text{ mW m}^{-2} \mu\text{m}^{-1}$) illumination levels, falling off to 91 nights per year at 75°N. At quarter-moon-equivalent ($0.4 \text{ mW m}^{-2} \mu\text{m}^{-1}$) illumination, there were 122 nights per year found at the equator and 52 nights per year at 75°N.

Comparing Figs. 6a,b reveals how the additional nights seen by the 0930/2130 orbit results in an increase for the combined observations for nearly all

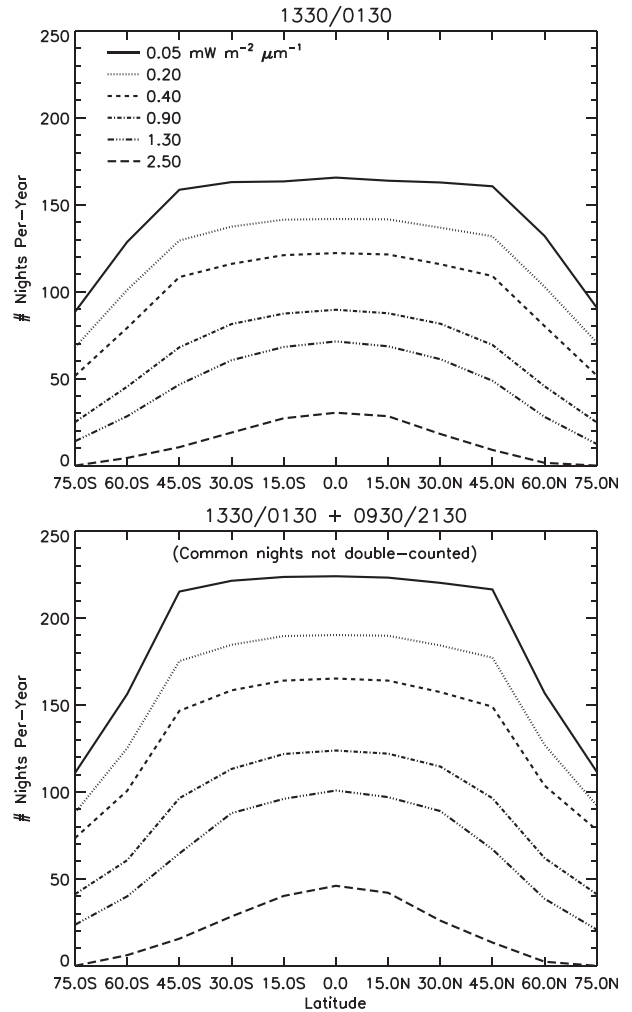


FIG. 6. SLAC model analysis of the number of nights per year containing values of lunar irradiance (weighted by cosine of the lunar zenith angle) that exceeds various thresholds, shown as a function of latitude. (top) Local observation times of 0130 and 1330, and (bottom) the additional lunar nights observed only at the 0930 and 2130 local times. Results are based on a 5-yr average from 2011 to 2015.

thresholds of lunar irradiance. For the combined results at the equator and crescent-moon-equivalent illumination there were over 223 nights per year, and roughly 165 nights per year at quarter moon. Thus, the number of available lunar nights in the tropics at crescent- and quarter-moon-equivalent illumination levels increased by 59 and 43, respectively, when including the 0930/2130 observations. The increase in available lunar nights is in addition to higher temporal resolution across a given night. Figure 6 indicates similar improvements for the combined observing system at midlatitudes, with a 39% mean increase of nights between 45°N and 45°S latitudes (averaged for all lunar thresholds shown).

7. Detailed simulation results for selected orbits

This section details the results of orbital simulations that account for the DNB swath and sensitivity in connection to the lunar geometry, phase, and irradiance. The analysis of section 6, while valid as a first-order approximation to the satellite-based lunar availability, does not account for the specific details of the satellite orbits of interest to this study. In particular, it does not account for the orbital inclination and the 3000-km-wide swath (the cross-track width of the image, defined by the orbital altitude and sensor scan angle limits), which results in a nonuniform distribution of local crossing times as a function of latitude. Nor does it account for the constant precession rate of the orbital plane, which leads to slight differences in the local crossing times over the course of the year. Accounting for these details is particularly relevant to near-terminator orbits, where, for example, an inclined orbit will traverse the terminator to different extents with season, and portions of a swath may cross into astronomical darkness even if the ground-track location itself is in twilight. Thus, our simulations must include sampling across the entire sensor swath.

The 1330, 1730, and 2130 orbital configurations [given in the form of two-line element (TLE) files that contain all the parameters necessary for orbital prediction] for the originally proposed NPOESS satellites were provided by the NPOESS Integrated Program Office (J. Furgerson 2008, personal communication). The 1330 orbit information is representative of the planned NPP and JPSS satellites. The model used for the orbital simulations is based on the classical theory of Keplerian orbits and the nonspherical gravitational perturbation of Earth for sun-synchronous orbital simulations, as outlined by Kidder and Vonder Haar (1995). The 1730 and 2130 orbits were analyzed here as well to determine the effectiveness of the original NPOESS constellation. In addition, two alternative terminator orbital configurations (1630 and 1830 LTAN) were simulated to examine sensitivity in this special case.

For each orbital configuration, simulations were run at 1-min time steps for 5-yr periods beginning at 0000 UTC 1 January 2011 and running through 2359 UTC 31 December 2015. The multiyear simulation was required to provide a sampling of the lunar cycle (which varies in phase from one month to the next, owing to its sub-monthly period) sufficient for depicting the zonally averaged simulation results at a monthly time resolution. The $\sim 6.7 \text{ km s}^{-1}$ satellite ground speed for these orbits translates to approximately 400-km spacing of the 1-min samples in the along-track direction. To account for the sensor swath in the statistics (most relevant to near-terminator simulations where the satellite ground track

may be in twilight conditions but swath edge is in astronomical darkness), cross-track sample points were included at $\pm 300, 600, 900, 1200,$ and 1500 km about nadir. As such, for a great circle Earth circumference of about $40\,000 \text{ km}$ there were 1100 samples per orbit, $15\,840$ samples per day, 5.7816×10^6 samples per year, and 2.8908×10^7 samples for the 5-yr simulation record of each satellite orbital configuration considered. Although the density of samples in the along- and cross-track dimensions of these simulations is far less than the native pixel resolution of the DNB, for the purposes of this statistical analysis it was sufficient for resolving the terminator (which varies on a scale of order 1000 km) and the associated structure of solar and lunar illumination. Because of the rapidly converging longitude lines at high latitudes, results poleward of about 60° must be interpreted with increasing caution because of degraded sampling, but are included here for completeness.

At each sample location in these orbital simulations, the following data were collected: location (latitude/longitude), date/time (UTC), solar and lunar altitude and azimuth angles, lunar phase function (ranging from 0 for new moon to 1 for full moon), solar and lunar illuminance (luxes), the lunar irradiance ($\text{mW m}^{-2} \mu\text{m}^{-1}$), and the lunar phase angle (180° when the moon eclipses the sun, and 0° at the antisolar point when the moon is eclipsed by Earth's shadow). The solar and lunar geometry, lunar phase function, and solar and lunar illuminance properties were computed by the SLAC model, and the lunar irradiance and phase angle were computed from the Miller and Turner (2009) model described in section 3. Lunar irradiances were weighted to the provisional sensor response function of the DNB (former Raytheon Santa Barbara Remote Sensing Group 2006, personal communication); thus, the results stratified by lunar irradiance presented herein are specific to this observing system. Since the principal objective of this research was to provide a quantitative space/time analysis of nighttime lunar availability at different thresholds of lunar illumination, only the sample locations, date/time information, solar/lunar altitude angles, and lunar irradiances were required.

Figure 7 shows the distribution of global nighttime lunar observations for the 1330 orbit as a function of the lunar phase angle ($0^\circ = \text{full moon}$, $180^\circ = \text{new moon}$), based on the full 5-yr simulation. For this orbital configuration, about 39% of all samples (translating to about 78% of the nighttime hemisphere samples, which include twilight samples) satisfied the astronomical dark criteria defining night for this study. The 1730 and 2130 orbits (not shown) provided about 28% and 76% of all nighttime samples, respectively. At a given point in the lunar cycle (i.e., traversing the horizontal axis of Fig. 7),

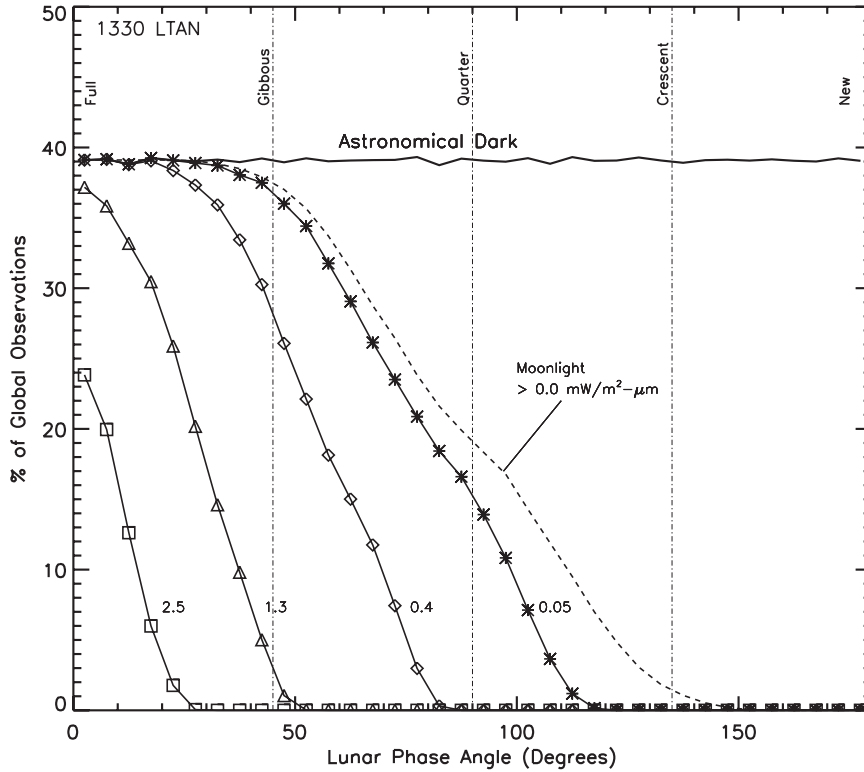


FIG. 7. Fraction of total (day and night) observations offering lunar irradiance above a given threshold, shown as a function of the lunar phase angle, for the 1330 LTAN orbital configuration (2011–15 orbital simulation).

the breakdown of lunar availability at various lunar irradiance thresholds is shown. Although the crescent moon begins at a 135° lunar phase angle, the first significant fractions of moonlight detected at the crescent-moon-equivalent illumination level of 0.05 mW m⁻² μm⁻¹ do not occur until the lunar phase angle has fallen below about 110°, a lag due to the effects of lunar zenith cosine weighting and the DNB response function. An additional detection lag, arising from the specific albedo properties of the target itself, is not shown. By the time in the lunar cycle when the phase angle has fallen below 50°, nearly all the available nighttime observations for this orbital configuration contain levels of moonlight at or above the equivalent-quarter-moon level of 0.4 mW m⁻² μm⁻¹.

To estimate the spatial/temporal frequency distribution of lunar nights encountered by a given orbital configuration, all nighttime samples of each simulation were extracted and binned as a function of location (by 5° latitudinal zones), time of year (by calendar months), and lunar irradiance threshold (weighted by cosine of lunar zenith angle and by DNB response function). These values were normalized by the total nighttime samples in each latitudinal zone and month, providing the fraction

(expressed in percentage) of lunar irradiance in excess of various thresholds.

Figure 8 shows the results of this procedure for the 1330, 1730, and 2130 orbits as a function of several lunar irradiance thresholds as well as the fraction of nonlunar nights. Since the orbits are sun-synchronous, the results apply to any given longitude around the globe. The seasonal cycle is clearly evident here, with voids of night observations during the polar summers. Where astronomical darkness prevails, the fraction of moon-free nights is close to 50% (for a fixed local time at a point on Earth’s surface, roughly half of the lunar orbit is observable). For lunar nights, when nighttime and the moon is above the horizon at the time of the satellite overpass, frequencies decrease with increasing values of lunar irradiance since the sample size is restricted to progressively smaller portions of the lunar cycle about the full moon. For the 1330 orbit and near the equator, the annually averaged percent of night samples is [45.1%, 33.4%, 19.2%] for the thresholds of [0.05, 0.4, 1.3] mW m⁻² μm⁻¹ shown in Fig. 8. Frequencies decrease with increasing latitude within a given month as well because of the lunar zenith angle weighting. Whereas the 1330 and 2130 orbits produce similar frequency-of-occurrence structures, we

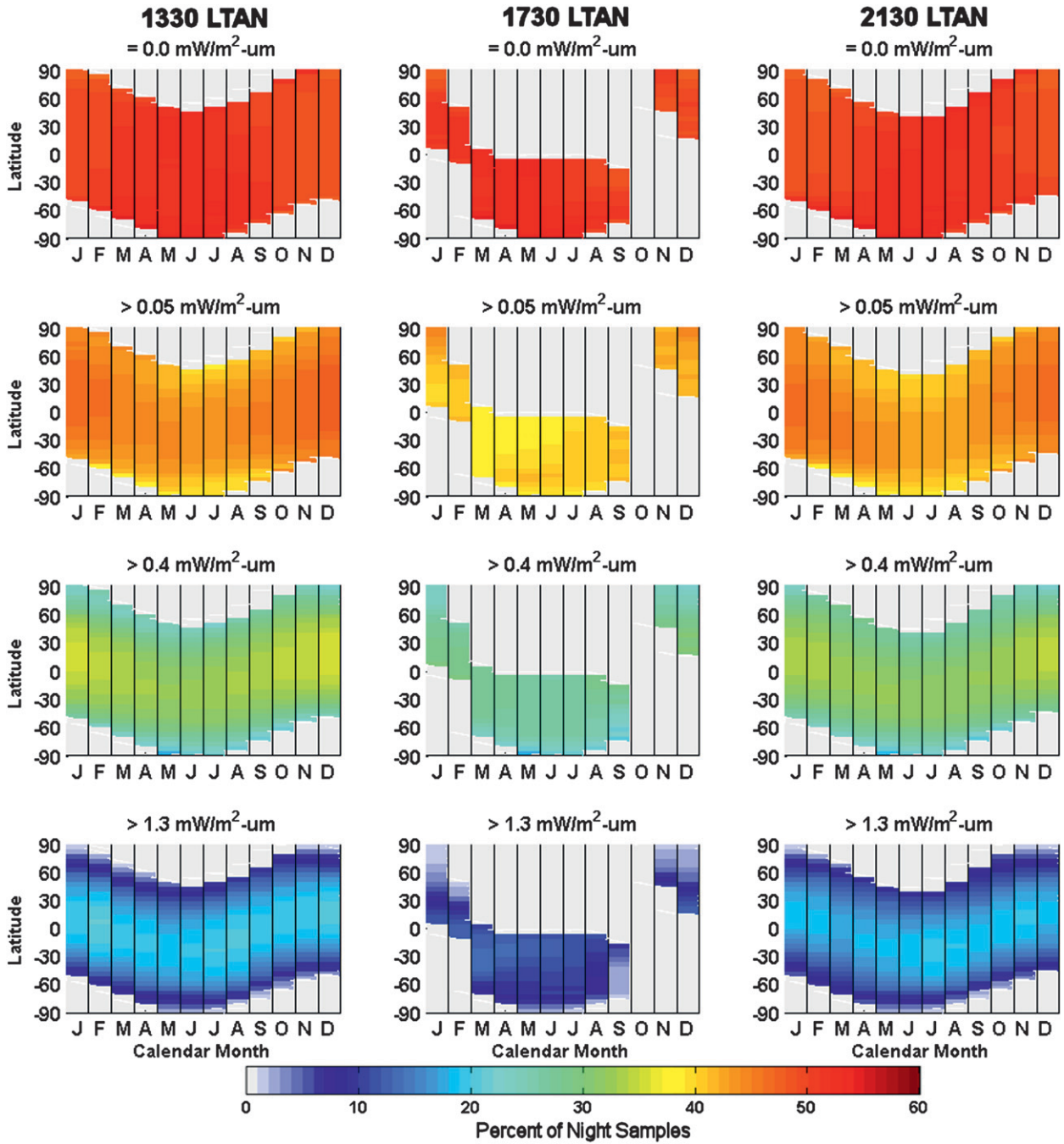


FIG. 8. Percent of all nighttime observations that (top) are moon free or (bottom rows) exceed selected lunar irradiance thresholds as a function of latitude and month for three different orbital configurations. Colors denote the percentage of nighttime samples at given latitude and given month that either contained (top) no moonlight or (bottom rows) moonlight at levels above a given threshold. Results based on 5-yr orbital simulations from 2011 to 2015.

recall from Figs. 5, 6 that important differences exist in terms of their sampling of the lunar cycle.

In contrast to the 1330 and 2130 orbits, there is a marked decrease in lunar availability for the 1730 orbit, including one month of the year (October) without any

lunar observations whatsoever. The void is due to a lack of astronomical dark observations at this time of the year for this particular orbital configuration—a topic that will be explored in more detail in the section to follow. The 1730 tendency toward more nighttime lunar

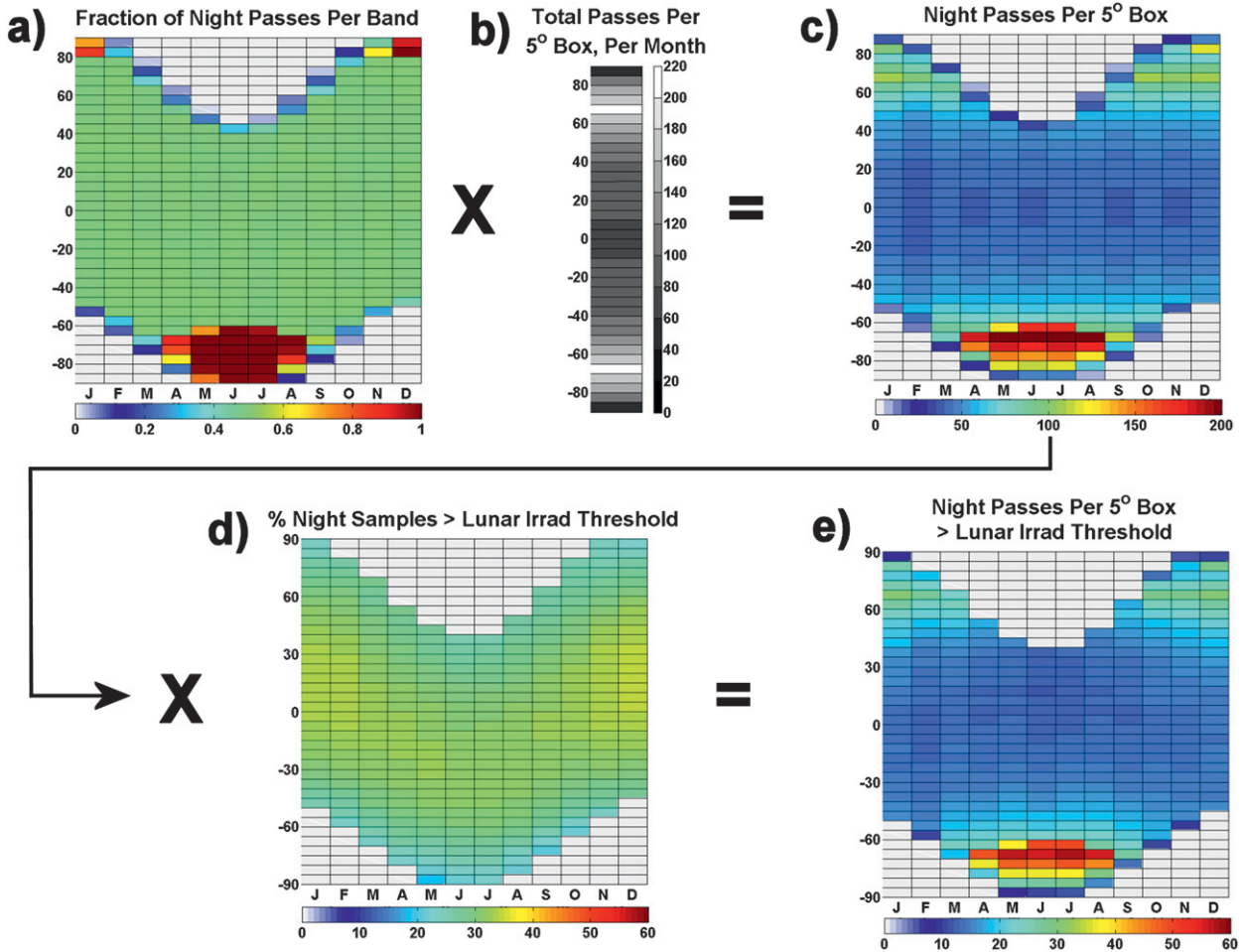


FIG. 9. Example of procedure for determining the number lunar-night satellite overpasses occurring within a 5° lat/lon box as a function of latitude and month of year (see text for details).

observations in the Southern Hemisphere is tied to the orbital inclination. This bias can be anticipated by inspecting Fig. 3, which shows how the VIIRS swath intercepts (and crosses) the terminator at a higher incident angle in the Southern Hemisphere winter than it does in the Northern Hemisphere winter.

Knowledge of the frequency of nighttime observations as shown in Fig. 8 does not translate directly to the actual number of lunar-night satellite overpasses expected at a given location. For this information, one must first know the actual number of nighttime satellite overpasses that pass through the latitude of interest, keeping in mind that the ground-track repeat pattern of sun-synchronous orbits is nonuniform, with the greatest density of overlapping passes found between latitudes of 55° and 80° (north and south). Additionally, knowing the number of lunar-night satellite overpasses expected to traverse a given subsection of a given latitudinal band (e.g., a 5° box) would be far more useful to planners

than knowing the total number of passes intercepting the 360° longitudinal span of the zonal band.

The number of lunar-night passes over a given region per month is illustrated in Fig. 9. For a given orbital configuration, we first calculated the total number of satellite passes through each 5° zonal band per month as well as the subset of those total passes that were night (astronomical dark, regardless of lunar illumination). A subtle detail of this calculation, important to higher latitude bands, was the tracking of ascending and descending orbit passes. This involved monitoring trends (increasing or decreasing) in ground-track latitude from one sample position to the next and defining new “passes” when inflection points were traversed. Dividing the number of night passes by the total number of passes provides the fraction of all passes in a zonal band (Fig. 9a) that are night. Next, each 5° zonal band was partitioned into a set of adjacent 5° × 5° boxes (i.e., 72 boxes), and the number of passes per 24-h period

through each box was determined based on a 16-day subset of the orbital simulation (this period captures all possible orientations of the swath across the satellite's ground-track repeat cycle). The average number of passes through a set of 5° boxes within each zonal band was computed, and these values were multiplied by the number of days in each month (Fig. 9b) to yield the number of nighttime passes per 5° box (Fig. 9c). Finally, we multiplied this number by the percentage of night samples exceeding a given lunar irradiance threshold (information of the kind shown in Fig. 8, and reproduced for the purpose of illustration in Fig. 9d). The final result (Fig. 9e) is the number of nighttime satellite overpasses per month within an arbitrary 5° box at a given latitude that contains moonlight detectable by the DNB in excess of a particular threshold.

Figure 10 shows the outcome of this procedure when applied to the 1330, 1730, and 2130 orbits at selected thresholds of lunar irradiance corresponding to no moon (top row), followed by crescent, quarter, and gibbous moons. The results indicate that for the 1330 and 2130 orbits, quarter-moon-equivalent or greater lunar illumination is available for about half the nighttime passes in each month in the tropics and midlatitudes. Specifically, the annual average number of lunar-night passes per month near the equator for the lunar thresholds of $[0.05, 0.4, 1.3] \text{ mW m}^{-2} \mu\text{m}^{-1}$ was $[17.9, 13.2, 7.7]$ for the 1330 orbit and $[17.5, 12.7, 7.1]$ for the 2130 orbit. The number of lunar-night passes per month is less than the total nights available in a typical calendar month (~ 30) because only the nights with moonlight (cosine weighted by the lunar zenith angle) exceeding the stated threshold are reported. Likewise, there are about 20 completely moonlight-free nighttime passes per month (corresponding to the top row of Fig. 10) in the tropics from both of these orbits.

The pass counts in Fig. 10 tend to grow with increasing latitude. We recall that night is not defined here in terms of whether or not there were astronomical dark conditions at the time of the satellite overpass (as opposed to a wall clock time). As such, the perpetually dark polar winter months contain significantly more night passes than the number of days in the typical calendar month, since both ascending and descending nodes are counted. The other cause for higher pass counts at higher latitudes is increased sampling by overlapping ground tracks. For the 1330 orbit, a peak number of 85 night passes occurs in the $65^\circ\text{--}70^\circ\text{S}$ band during May–July for the $0.05 \text{ mW m}^{-2} \mu\text{m}^{-1}$ lunar threshold. Noteworthy attributes of the 1730 orbit, in contrast to the 1330 and 2130 results, include the relative scarcity of tropical coverage and midlatitudes of the Northern Hemisphere, the lack of any passes during the month

of October, and the relatively high values in the polar winter (particularly in the Southern Hemisphere at mid-latitudes). The following section looks into these interesting near-terminator orbit characteristics in more detail.

8. Sensitivity of near-terminator orbits

It is clear from Fig. 3 that the near-terminator orbits will be subject to enormous nighttime/lunar variability across space and time. Specifically, the DNB swath may either straddle the terminator or cross into pure day or night conditions, with significant variation in this behavior over the course of seasons and latitude. Understanding this detail is particularly relevant for the planning of future satellite missions in near-terminator orbits where first light imaging is required (DMSP has flown near-terminator orbits for over 50 yr). In this section, we examine changes in lunar availability as a function of LTAN changes (± 1 h) to the originally planned NPOESS orbit of 1730 LTAN. Our strict definition of what defines night precludes the consideration of twilight observations, although such illumination might be useful for cloud/aerosol detection among other environmental applications.

To better understand the relationship between LTAN and the number of observations encountered in the dark portion of the Earth, we took a simple geometric approach. Shown in Fig. 11 is the angle formed between the vector normal to the satellite's orbital plane and the vector connecting the center of Earth to the sun. This angle is contoured as a function of time of year and LTAN value. Where the angle is near 90° , an instrument viewing at nadir would observe the maximum possible number of points in the dark because it crosses the terminator at a 90° angle in each orbit. Where the angle is 0° or 180° , the satellite orbits above the terminator (i.e., ground track of the satellite coincides with the great circle of the terminator), and a nadir-viewing instrument would only observe twilight conditions. Overlaid in Fig. 11 are horizontal lines denoting LTAN for various sun-synchronous orbits.

The VIIRS/DNB collects observations not only at nadir but across a 3000-km swath, which translates to roughly 13.5° in great circle distance on either side of the ground track. Astronomical dark, however, does not occur until 18° into the dark side of the terminator. For such a swath width, if the satellite ground track were directly atop the day/night terminator, then the night side of the swath would not reach into the astronomical darkness. We can visualize this by considering the angle formed between two vectors: one that points from the Earth to the sun and another that is normal to the

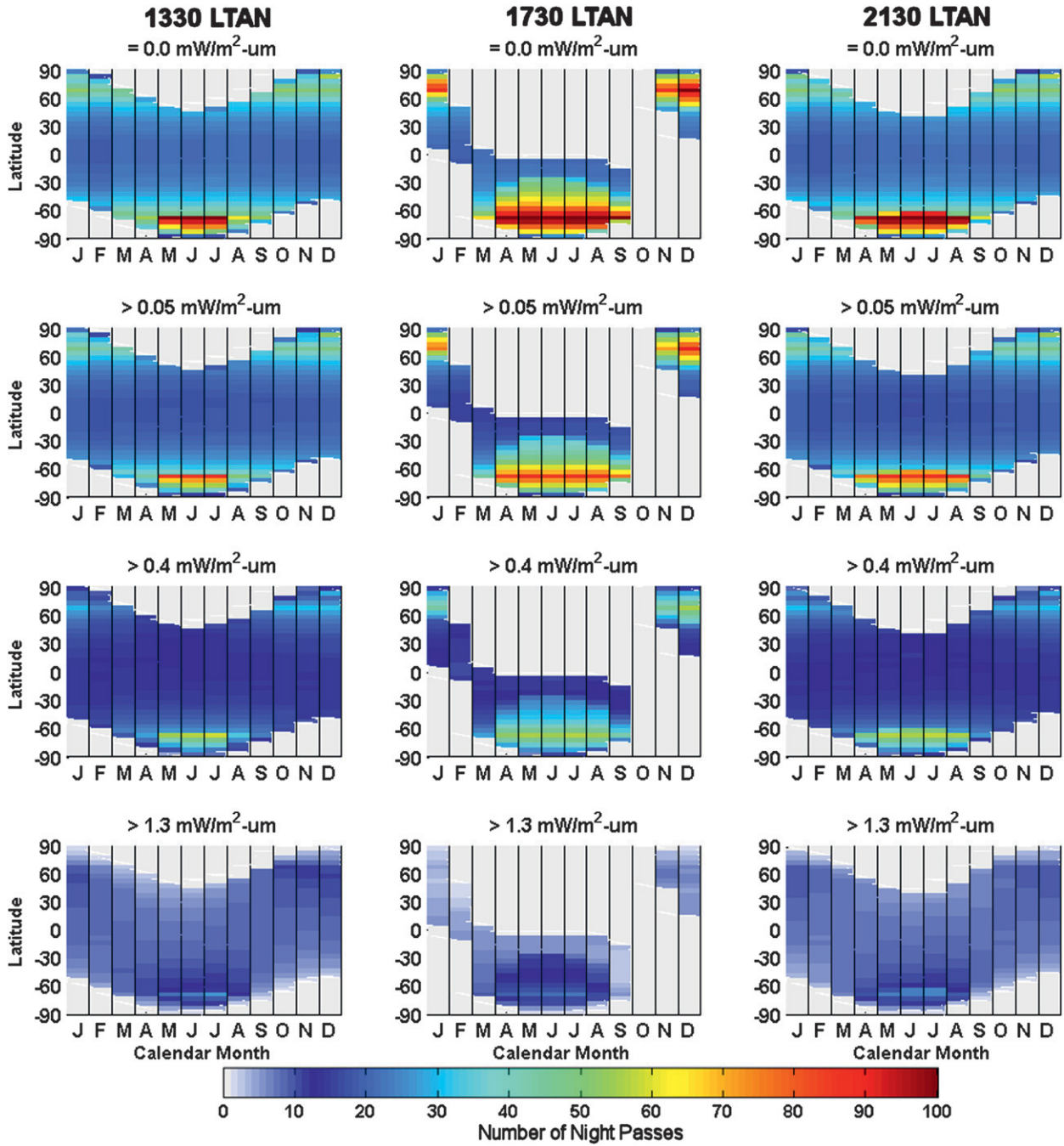


FIG. 10. The results of the procedure in Fig. 9 applied to the 1330, 1730, and 2130 LTAN orbits.

satellite’s orbital plane. If these two vectors are parallel (i.e., forming angles of 0° or 180°), then the satellite ground track is directly atop the terminator, and if the vectors are normal, then the satellite has equatorial crossing times of local noon and midnight. We will refer to this here as the “terminator angle.” For a satellite in a near-terminator orbit, if the terminator angle is close to either 0° or 180° , then potentially no part of its swath

will reach astronomical darkness, depending on the swath width. For the VIIRS/DNB swath width, this critical terminator angle is either less than 4.5° (below which a $\sim 13.5^\circ$ wide half-swath would not reach the critical astronomical dark threshold of 18°) or is greater than 175.5° (i.e., for the opposite node of the orbit). As the terminator angle for a particular LTAN orbit approaches the critical value, there will be progressively

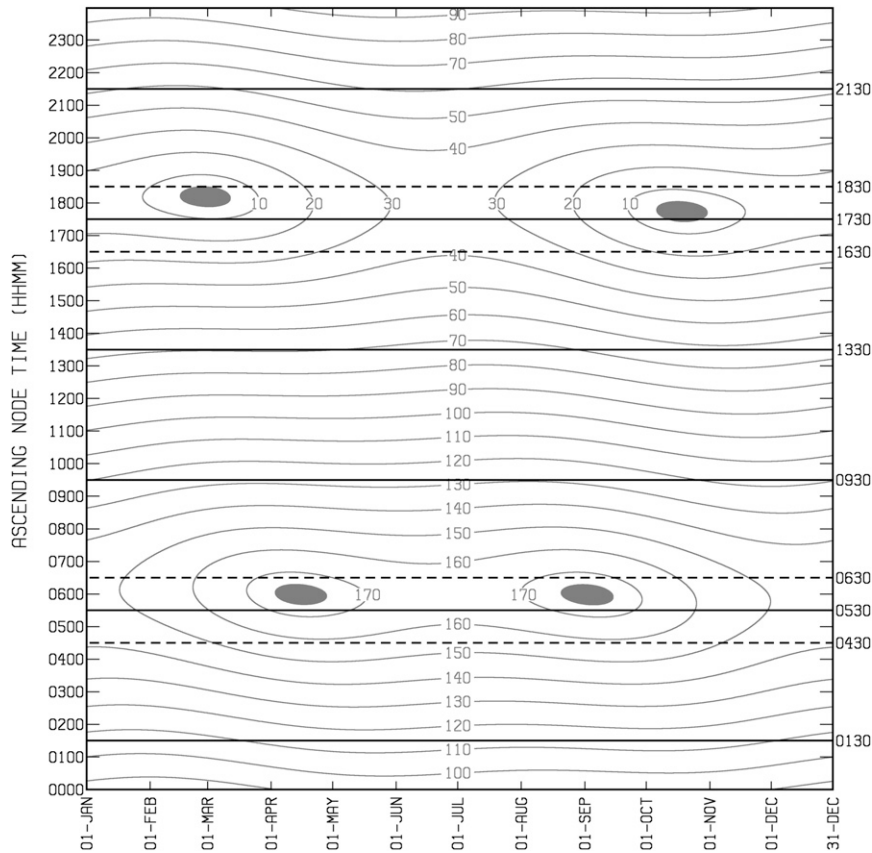


FIG. 11. Terminator angle (degrees) contoured as a function of LTAN and time of year. Ascending node local times for various orbital configurations of interest are drawn as horizontal lines. Critical values less than 4.5° or greater than 175.5° are shaded, representing regions where the VIIRS/DNB would offer no pure-night observations.

smaller portions of the sensor swath reaching astronomical darkness. From the standpoint of pure nighttime applications where astronomical darkness is required, these regions define “keep-out zones” when considering various LTAN orbits.

Figure 11 visualizes the terminator angle as a function of different satellite LTANs and times of year. The areas shaded in gray represent regions where astronomical darkness observations from a sensor with swath width similar to the VIIRS/DNB would be unattainable; these are the keep-out zones described above. Specific LTANs of interest to this study are highlighted as horizontal lines. For example, a DNB aboard a 1730 LTAN satellite would not observe any astronomical darkness between 12 and 27 October. The top row of Fig. 12 shows the ascending and descending nodes of the 1730 orbit at a midpoint in this period, 19 October, when it is most closely aligned with the terminator, illustrating how the DNB swath does not extend into the astronomically dark portion of the nighttime hemisphere. These geometrically based keep-out zones help explain

the lack of nighttime passes reported for the 1730 orbit, referring back to Fig. 10.

Since there is a minimum of astronomical dark observations in October, one might also expect to find a corresponding minimum near the vernal equinox when exactly the same declination angle is encountered and terminator orientation is produced. Surprisingly, Fig. 11 indicates that while there is indeed another minimum in the March timeframe, it is shifted slightly earlier in local time and thus does not eliminate as many dark-night observations. The lower-right panel of Fig. 12 confirms that on 3 March, the day of spring minimum, there are astronomically dark observations during the descending portion (0530) of the 1730 orbit. The equation of time, which describes the east and west extents of the analemma mentioned in section 4, explains this asymmetry. Here, the satellite orbit’s constant precession rate about the Earth (tracking the *mean* solar time) differs from the variable angular velocity of Earth as the planet traverses its elliptical orbit about the sun. Thus, slightly different

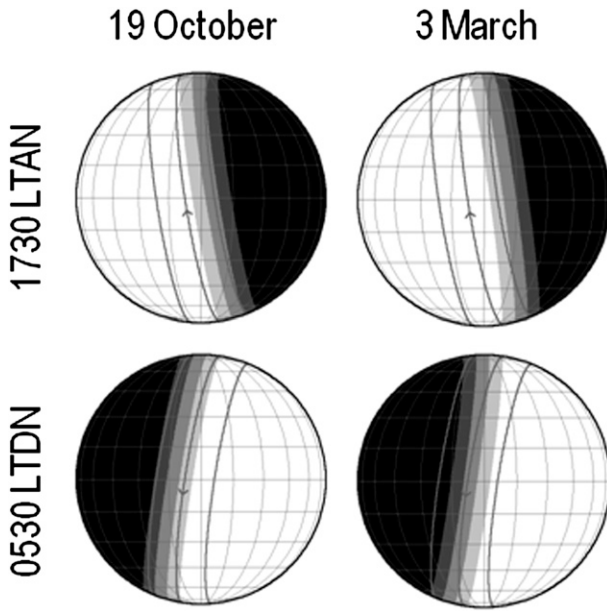


FIG. 12. As in Fig. 2, but for 19 Oct and 3 Mar, when the 1730 orbit is most closely aligned with the terminator. The configuration provides few opportunities for astronomically dark (night) observations across the VIIRS/DNB swath in March, and none whatsoever in October.

apparent solar times occur for a satellite LTAN over the course of the year, accounting for the slight seasonal asymmetries of the dark-night unobservable zones shown in Fig. 11.

A question germane to the analysis of near-terminator orbit sensitivity is how the lunar availability might change in response to a shift of the orbital plane (i.e., modifying the “right ascension of the ascending node” orbital parameter), increasing sampling of the darker side of the terminator. Casting this question in terms of a practical example, would adjusting the 1730 orbital plane to a slightly different LTAN enable more astronomical dark observations (and thereby more opportunities for lunar applications) while maintaining the near-terminator twilight imaging capabilities? To address this question, we modified the 1730 orbital parameters to result in a ± 1 -h shift (i.e., producing 1630 and 1830 LTAN orbits) and reran the 5-yr simulations (Figs. 13, 14). Comparing these orbits with the 1730 orbit shown in Fig. 3, we see that these relatively small LTAN shifts (translating to $\pm 15^\circ$ shifting of the nodes) result in very different terminator sampling behaviors.

Comparisons of the percentage of nighttime samples (analogous to Fig. 8) and the corresponding number of nighttime passes (analogous to Fig. 10) that exceed selected lunar irradiance thresholds for the 1630, 1730, and 1830 orbits are shown in Figs. 15, 16, respectively. There are many lunar observations in the polar winters, with

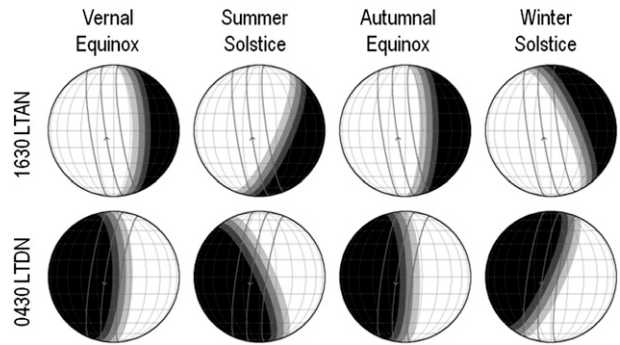


FIG. 13. As in Fig. 3, but for a satellite with a 1630 LTAN. The 0430 descending node provides significantly more astronomical darkness coverage while maintaining terminator coverage in the NH.

a bias toward higher Southern Hemisphere values, owing to the inclination of these terminator orbits (which intrude on earlier-dawn local times in the descending node). The data voids, related to the equation of time as explained above, are present for both the 1730 (October) and 1830 (February) orbits, but not for the 1630 orbit. As before, the voids correspond to periods when the satellite’s orbit matches very closely with the line of the terminator and the DNB swath does not extend into astronomical dark regions. Inspection of Fig. 11 confirms the presence of a springtime void for LTAN values near 1830 and the progression away from both spring and fall keep-out zones for the 1630 orbit.

Perhaps the most striking result is that shifting the orbit to an LTAN an hour earlier than what was originally proposed the early morning NPOESS orbit would result in a dramatic improvement to lunar availability at midlatitudes. Results analogous to Fig. 7 (not shown) indicate that 48% of nighttime hemisphere samples for the 1630 orbit are in astronomical darkness (in contrast to the 28% for the 1730 orbit). This is in strong contrast to a shift to the later 1830 orbit, which offers no quantitative improvements over the 1730 orbit.

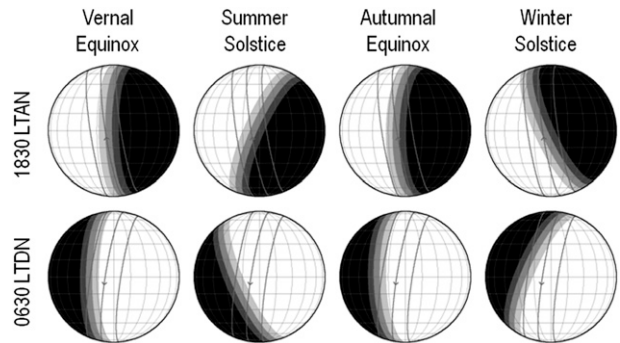


FIG. 14. As in Fig. 3, but for a satellite with an 1830 LTAN. Nighttime coverage is similar to the 1730 LTAN orbit.

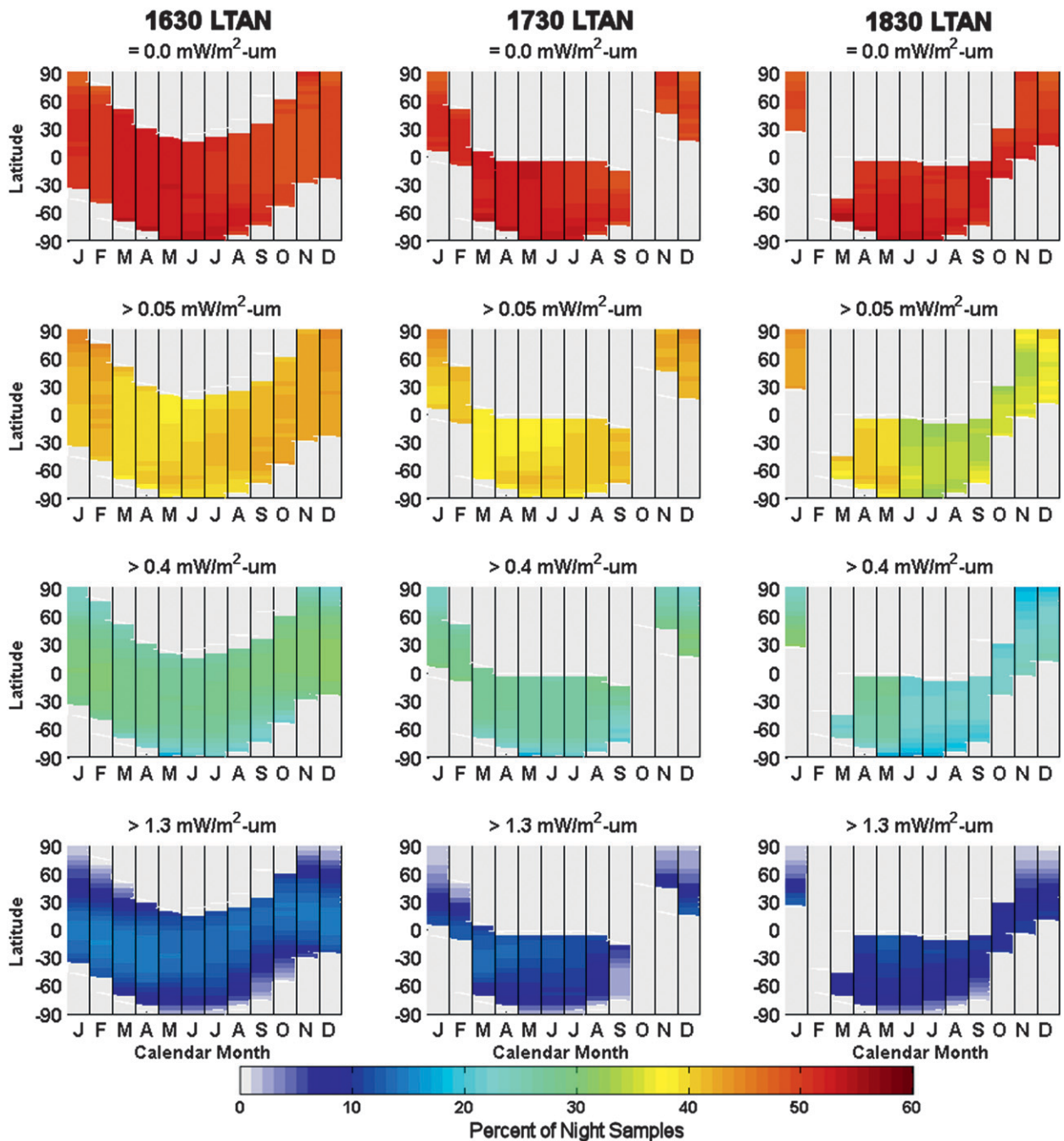


FIG. 15. As in Fig. 8, but for a comparison between 1630, 1730, and 1830 LTAN near-terminator orbits.

Based on the width of the DNB swath and its multi-stage gain configuration, the 1630 orbit would still provide dawn–twilight (first light) imagery and would also cover more astronomical darkness, thereby taking better advantage of the high-gain amplification stage of the DNB sensor. Here, when the moon is above the horizon (particularly during the last quarter of the lunar

cycle, when the moon is near zenith at dawn), moonlight applications could be pursued without the complications of twilight contamination. Likewise, when the moon is below the horizon, terrestrial visible light emission-based applications (e.g., stable light monitoring) would be available in the astronomically dark parts of the DNB swath. Furthermore, since the 1630 LTAN

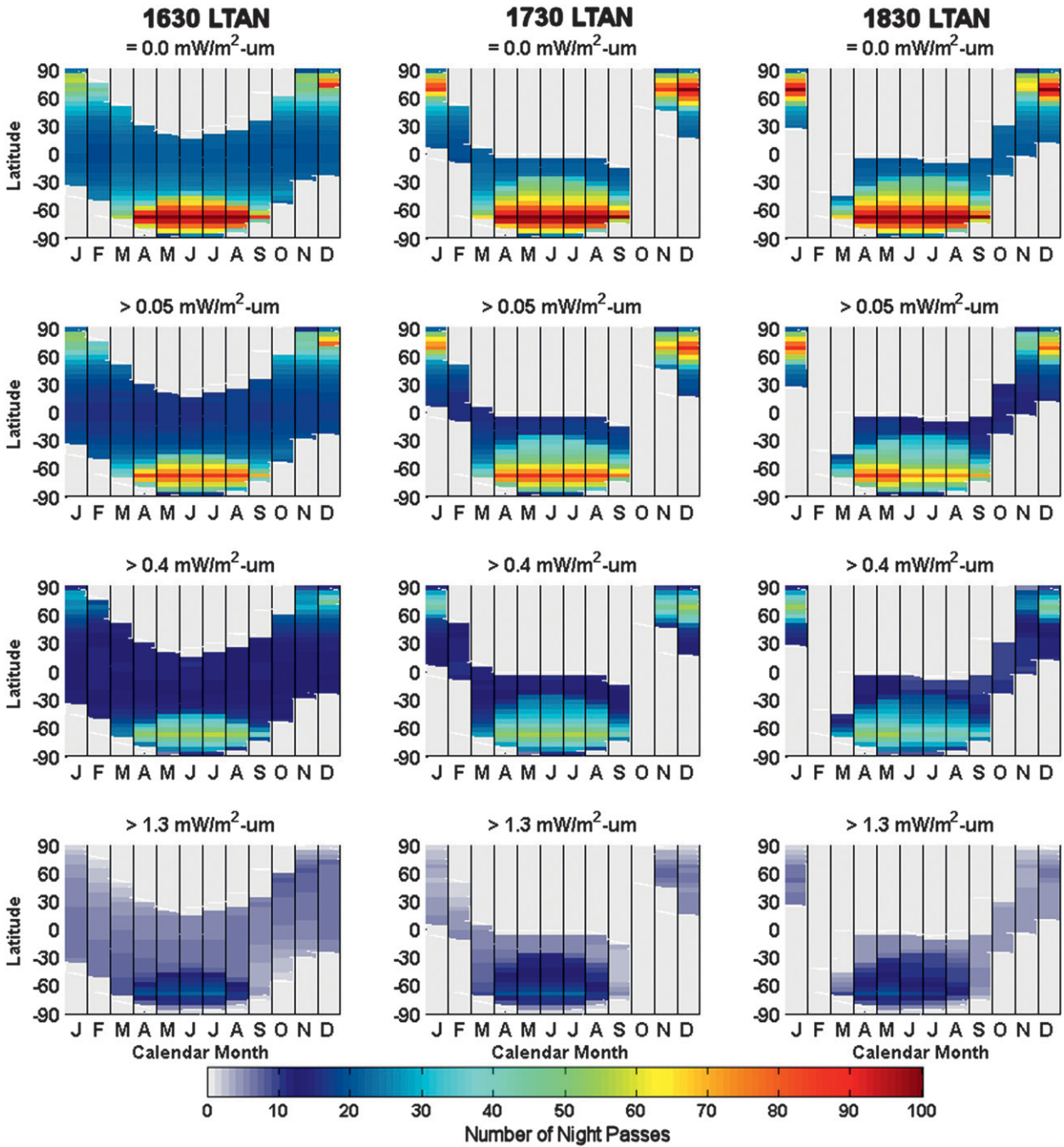


FIG. 16. As in Fig. 10, but for a comparison between 1630, 1730, and 1830 LTAN near-terminator orbits.

orbit would offer more astronomical dark observations, it by definition would also offer more pure-day (late afternoon) observations on the descending node of the orbit. This late-afternoon pass would therefore take better advantage of the other multispectral daytime bands on VIIRS that require higher levels of solar signal than the DNB.

9. Summary and conclusions

We have conducted an analysis of nighttime lunar availability within the context of various planned and recommended sun-synchronous satellite orbits. The objective of this work was to provide a quantitative assessment of when and where on Earth the new quantitative

applications enabled by the VIIRS/DNB will apply (both lunar and nonlunar nighttime applications) based on detailed 5-yr orbital simulations coupled to a lunar irradiance model. The hope is that the information will be helpful to both research and operational users in planning various activities that incorporate low-light visible observations, as well as to the architects of future satellite missions.

The immediate focus of the research was on the 1330 LTAN orbit scheduled to carry the VIIRS/DNB on NPP and JPSS. For this orbit, sufficient moonlight for quantitative low-light visible applications occurs for roughly one-half to one-third (crescent- to quarter-moon-equivalent illumination levels) of all nights at midlatitudes and the tropics. The remaining nights provide opportunities for terrestrial light emission applications. The lunar-night availability is a strong function of season and latitude, particularly at high latitudes where the effects of lunar zenith and Earth's declination manifest in lower irradiance and periods of extended daylight/darkness. The results were translated to the expected number of passes over a given region, taking into account the swath width and orbital configuration, which results in significantly higher revisit rates at higher latitudes.

Other orbital configurations were considered as well, with the 1730 and 2130 LTAN orbits selected to demonstrate the original NPOESS observing system concept and possible future missions that may complement JPSS. It was shown that adding a 2130 orbit provided similar lunar availability to the 1330 orbit, but with the distinction of roughly a third of those nights being additional—the result of waxing-phase moons that are above the horizon at the time of the 2130 local time overpass but have set in the western horizon prior to the 0130 overpass. This illustrates the important point that a constellation provides not only improved temporal refresh on a given night but also a more complete sampling of the lunar cycle, yielding additional moonlit nights.

A special focus was placed on the near-terminator orbit region, where low-light imagery via the DMSP/OLS has occurred for decades and the likelihood of a DNB-like sensor joining this orbit in the future seems high. Significantly fewer lunar nights were encountered in this orbit, including a period in October when no observations occurred in astronomical darkness. The orbital simulations were reproduced for 1630 and 1830 LTAN, revealing a marked improvement to lunar availability in the former and no improvement in the latter. Specifically, the 1630 orbit would provide nearly double the number of samples observed in astronomical darkness in comparison to the 1730 or 1830 orbits. The pronounced seasonal asymmetries of the 1730 and 1830

orbits are the result of the equation of time (arising from the nonuniform angular rotation rate of the Earth about the sun). These results suggest that an optimal sun-synchronous orbit satisfying both twilight and pure-night low-light imaging requirements (taking advantage of all three gain stages of the DNB sensor) would be somewhat earlier than 1730 LTAN.

In the near term, the NPP and JPSS satellites, together with the legacy OLS on DMSP, will compose the constellation of low-light visible sensors. The analysis of the midevening and terminator orbits was intended to assist planners of future satellite missions that may include low-light visible sensors (e.g., PostEPS in the 2130 orbit). The inclusion of the other orbits originally planned as part of the NPOESS constellation is important not only from the standpoint of capturing additional lunar nights, but also for the observation of diurnally sensitive parameters. Afternoon convection, wild land fires, and dust storms (e.g., Membery 1983; Miller et al. 2008) are examples of diurnally locked phenomena that tend to emerge in the late afternoon and persist into the early evening hours, potentially observable by the 2130 orbit. Furthermore, bioluminescent milky seas (e.g., Herring and Watson 1993), a phenomenon whose temporal characteristics are generally unknown, were first detected from space by a midevening (~2030 local time) DMSP orbit (Miller et al. 2005a). For these and other parameters, a constellation of low-light visible sensors would significantly expand the horizons of environmental characterization.

Acknowledgments. The support of the research sponsors, the Oceanographer of the Navy through the program office at the PEO C4I & Space/PMW-180 under Program Element PE-0603207N, the Office of Naval Research under Program Element PE-0602435N, and the NPOESS Integrated Program Office located in Silver Spring, MD, is gratefully acknowledged. We thank Mr. John Bangert of the U.S. Naval Observatory for assistance with the SLAC model, and Mr. John Furgerson of NOAA for providing the two-line element data used in these simulations.

REFERENCES

- Allison, L. J., Ed., 1980: Meteorological satellites. NASA Tech. Memo. 80704, 84 pp.
- Brown, D. R. E., 1952: Natural illumination charts. Dept. of the Navy, Bureau of Ships Rep. 374-1, Project Ns-714-10, Washington, DC, 47 pp.
- Buratti, B. J., J. K. Hillier, and M. Wang, 1996: The lunar opposition surge: Observations by Clementine. *Icarus*, **124**, 490–499.
- Christian, H. J., K. T. Driscoll, S. J. Goodman, R. J. Blakeslee, D. A. Mach, and D. E. Buechler, 1996: The Optical Transient Detector (OTD). *Proc. 10th Int. Conf. on Atmospheric Electricity*,

- Osaka, Japan, International Commission on Atmospheric Electricity, 368–371.
- , and Coauthors, 1999: The Lightning Imaging Sensor. *Proc. 11th Int. Conf. on Atmospheric Electricity*, Guntersville, AL, International Commission on Atmospheric Electricity, 746–749.
- Dickinson, L. G., S. E. Boselly, and W. S. Burgmann, 1974: Defense Meteorological Satellite Program (DMSP) user's guide. Air Weather Service (MAC), U.S. Air Force Rep. AWS-TR-74-250, 109 pp.
- Ebener, S., C. Murray, A. Tandon, and C. Elvidge, 2005: From wealth to health: Modeling the distribution of income per capita at the sub-national level using nighttime lights imagery. *Int. J. Health Geogr.*, **4**, 5–14.
- Elvidge, C. D., K. E. Baugh, E. A. Kihn, H. W. Kroehl, and E. R. Davis, 1997: Mapping city lights with nighttime data from the DMSP Operational Linescan System. *Photogramm. Eng. Remote Sens.*, **63**, 727–734.
- , and Coauthors, 2007: The Nightsat mission concept. *Int. J. Remote Sens.*, **28** (12), 2645–2670.
- Fett, R. W., W. A. Bohan, J. J. Bates, and S. L. Tipton, 1983: Navy tactical applications guide: Operational environmental satellites. Naval Environmental Prediction Research Facility Tech. Rep. 83-02, 70 pp.
- Foster, J. L., and D. K. Hall, 1991: Observations of snow and ice features during the polar winter using moonlight as a source of illumination. *Remote Sens. Environ.*, **37**, 77–88.
- Herring, P. J., and M. Watson, 1993: Milky seas: A bioluminescent puzzle. *The Mar. Obs.*, **63**, 22–30.
- Johnson, D. B., P. Flament, and R. L. Bernstein, 1994: High-resolution satellite imagery for mesoscale meteorological studies. *Bull. Amer. Meteor. Soc.*, **75**, 5–33.
- Kidder, S. Q., and T. H. Vonder Haar, 1995: *Satellite Meteorology: An Introduction*. Academic Press, 466 pp.
- Kieffer, H. H., and T. C. Stone, 2005: The spectral irradiance of the Moon. *Astron. J.*, **129**, 2887–2901.
- Lee, T. F., S. D. Miller, F. J. Turk, C. Schueler, R. Julian, S. Deyo, P. Dills, and S. Wang, 2006: The NPOESS/VIIRS day/night visible sensor. *Bull. Amer. Meteor. Soc.*, **87**, 191–199.
- Lieske, R. W., 1981: DMSP primary sensor data acquisition. *Proc. Int. Telemetry Conf.*, Vol. 17, San Diego, CA, International Foundation for Telemetry, 1013–1020.
- Membery, D. A., 1983: Low level wind profiles during the Gulf Shamal. *Weather*, **38** (1), 18–24.
- Miller, S. D., and R. E. Turner, 2009: A dynamic lunar spectral irradiance dataset for NPOESS/VIIRS Day/Night Band nighttime environmental applications. *IEEE Trans. Geosci. Remote Sens.*, **47**, 2316–2329, doi:10.1109/TGRS.2009.2012696.
- , S. H. D. Haddock, C. Elvidge, and T. F. Lee, 2005a: Detection of a bioluminescent milky sea from space. *Proc. Natl. Acad. Sci. USA*, **102**, 14 181–14 184, doi:10.1073/pnas.0507253102.
- , T. F. Lee, F. J. Turk, A. P. Kuciauskas, and J. D. Hawkins, 2005b: Shedding new light on nocturnal monitoring of the environment with the VIIRS day/night band. *Atmospheric and Environmental Remote Sensing Data Processing and Utilization: Numerical Atmospheric Prediction and Environmental Monitoring*, H.-L. A. Huang et al., Eds., International Society for Optical Engineering (SPIE Proceedings, Vol. 5890), doi:10.1117/12.619534.
- , A. P. Kuciauskas, M. Liu, Q. Ji, J. S. Reid, D. W. Breed, A. L. Walker, and A. A. Mandoos, 2008: Haboob dust storms of the southern Arabian Peninsula. *J. Geophys. Res.*, **113**, D01202, doi:10.1029/2007JD008550.
- Oliver, B. M., 1972: The shape of the analemma. *Sky & Telescope: The Essential Magazine of Astronomy*, July Feature, 20–22.
- Sutton, P., D. Roberts, C. Elvidge, and K. Baugh, 2001: Census from Heaven: An estimate of the global population using night-time satellite imagery. *Int. J. Remote Sens.*, **22**, 3061–3076.
- Toenges-Schuller, N., and Coauthors, 2006: Global distribution pattern of anthropogenic nitrogen oxide emissions: Correlation analysis of satellite measurements and model calculations. *J. Geophys. Res.*, **111**, D05312, doi:10.1029/2005JD006068.
- Zhang, J., J. S. Reid, S. D. Miller, and F. J. Turk, 2008: Strategy for studying nocturnal aerosol optical depth using artificial lights. *Int. J. Remote Sens.*, **29**, 4599–4613.